Transp Porous Med
DOI 10.1007/s11242-006-9062-7

ORIGINAL PAPER

NMR for equilateral triangular geometry under conditions of surface relaxivity—analytical and random walk solution

Jan Finjord · Aksel Hiorth · Unn H. a Lad · Svein M. Skjæveland

Received: 03 November 2005/Accepted: 13 September 2006

Abstract We consider analytical and numerical solution of NMR relaxation under the condition of surface relaxation in an equilateral triangular geometry. We present an analytical expression for the Green's function in this geometry. We calculate the transverse magnetic relaxation without magnetic gradients present, single-phase, both analytically and numerically. There is a very good match between the analytical and numerical results. We also show that the magnetic signal from an equilateral triangular geometry is qualitatively different from the known solution: plate, cylinder, and sphere, in the case of a nonuniform initial magnetization. Nonuniform magnetization close to the sharp corners makes the magnetic signal very fast multiexponential. This type of initial configuration fits qualitatively with the experimental results by Song (*Phys. Rev. Lett*. **85**, 3878 (2000)), Song et al. (*Nature* **406**, 178 (2000)), Song (*Mag. Reson. Imag*. **19**, 417 (2001)) and Lisitza and Song (*Phys. Rev. B* **65**, 172406 (2002)). It should also be noted that the solution presented here can be used to describe absorption of a chemical substance in an equilateral triangular geometry (for a stationary fluid).

Keywords CPMG NMR · Diffusion · Equilateral triangle · Random walk · Analytical

1 Introduction

In the oil industry there has been a great interest in using NMR as a tool for improved reservoir characterizing. NMR can be used as an in situ tool for measuring oil and brine content in saturated porous rocks (Freedmann et al. 2002, Heaton et al. 2002,

A. Hiorth (✉) · U.H. a Lad
RF-Rogaland Research, P. O. Box 8046, N-4068 Stavanger, Norway
e-mail: ah@rf.no

J. Finjord · S.M. Skjæveland
University of Stavanger, N-4036 Stavanger, Norway

Hürlimann et al. 2002, Hürliman and Venkataramanan 2002). The distribution of oil and water in the porous rock is also very important. If a phase is in contact with pore wall, it will experience enhanced relaxation (Brownstein and Tarr 1977, 1979). One way of observing this is by studying how the oil signal changes when the core is aged (see Howard 1998; Zhang et al. 2000), and the references therein. The distribution of oil and water in a porous rock is mainly determined by the geometry of the pore space and the chemical composition of oil, brine and rock. The NMR signal from a porous rock will then be a strong function of the specific pore geometry and the wetting status of the rock. Experiments on porous rocks are well suited for showing an effect of enhanced surface relaxation due to wettability change. However, by study simpler systems, more information can be gained in order to understand how chemical properties will affect the magnetic signal.

By assuming a specific geometry for the porespace more information from the NMR signal can be obtained. Cylindrical and spherical geometries can be used when wettability is not a topic. However most reservoirs are mixed wet and one need geometries containing sharp corners. This realization is the starting point for this work. One of the simplest geometries, which allows for more than one phase to form a stable configuration is an equilateral triangular geometry. A great deal of attention have been devoted to triangles in order to understand the multiphase behavior of porous rocks (Radke et al. 1992, Mason and Morrow 1991, Morrow and Mason 2001). Triangles are the basic building blocks in pore network models (Jackson et al. 2002, Piri and Blunt 2002, Hui and Blunt 2000) and also bundle of equilateral triangular tubes models have been studied extensively (van Dijke and Sorbie 2003, Helland and Skjæveland 2002). Attempt of using a bundle of equilateral triangular tubes in interpreting NMR signal froms porous rocks have also been done (Al-Mahrooqi et al. 2004).

As always with NMR experiments the key challenge is to get a proper interpretation of the magnetic signal. The crucial step in order to gain precise knowledge from NMR signal is to have a good theoretical description of the magnetic signal. This work will only be concerned with magnetic signal from single phases, but it forms a necessary basis in developing numerical code for magnetic signal from triangles containing multiphases. The numerical solution presented in this work can be extended to account for more than one phase inside the rock and analytical single phase results is necessary in order to calibrate the numerical algorithm. The multiphase numerical code can then be used to study how wettability will influence the magnetic signal in a well defined geometry. Experiments on glass triangular tubes are in progress at our group and the analytical solution presented here will be used to interpret the experimental result, this will be considered in a different work.

The higher modes presented here are usually neglected, but have been shown to give valuable information of pore sizes (Song 2000a, Song et al. 2000b, Song 2001, Lisitza and Song 2002, Marinelli et al. 2003). In order to fully characterize a geometry one need information from higher modes. The lowest mode is dependent on the surface relaxivity and proportional to the internal surface area divided by the total volume of the pore (S/V), the higher modes are independent of the surface relaxivity and proportional to $(S/V)^2$. A clever way of enhancing the weight of the higher modes is by creating a nonuniform initial magnetization, as described by Song (2000a), Song et al. (2000b), Song (2001) and Lisitza and Song (2002).

The outline of the papers is as follows: in Sect. 2, we present the theory for magnetic relaxation in a confined space. In Sect. 3, we calculate the Green's function for an equilateral triangular geometry and in Sect. 4 we calculate the magnetization for

different initial configurations. Then we present details of the random walk solution in Sect. 5 and finally conclusion and discussion.

2 Theory

The equilateral triangular geometry is a true two-dimensional system, contrary to plate, cylinder and sphere geometry, first considered by Brownstein and Tarr (1979). This problem is much harder to solve, the technical reason for this is that it is not possible to choose a coordinate system where the axes are parallel to the sides of the triangle. Fortunately the calculation greatly simplifies because of a series of recent papers by Mccartin, which solves the diffusion equation in an equilateral triangular geometry (Mccartin 2002, 2003, 2004). The magnetization as a function of time is given by the following equations (Brownstein and Tarr 1977, 1979):

$$\frac{\partial M(\mathbf{r},t)}{\partial t} = D\nabla^2 M(\mathbf{r},t) - \frac{M(\mathbf{r},t)}{T_{2b}}\,. \tag{1}$$

T_{2b} is the bulk relaxation and D the diffusion constant. At the surface, Σ, we have the following boundary condition:

$$D\hat{\mathbf{n}}\cdot\nabla M(\mathbf{r},t) + \rho M(\mathbf{r},t)|_{\mathbf{r}=\Sigma} = 0\,, \tag{2}$$

where $\hat{\mathbf{n}}$ is the outward normal and ρ the surface relaxivity. Equation 1 (with $1/T_{2b} = 0$) and (2) are identical to the equations governing absorption of a chemical substance on a surface, in the case of a stationary fluid. The magnetization of the sample is:

$$M(t) = \int_{\Delta} \mathrm{d}\mathbf{r}\, M(\mathbf{r},t)\,, \tag{3}$$

where the integral is taken over the triangular domain. By introducing the Green's function we can write the magnetization as:

$$M(\mathbf{r},t) = \mathrm{e}^{-t/T_{2b}} \int_{\Delta} \mathrm{d}\mathbf{r}'\, \rho(\mathbf{r}') G(\mathbf{r}'|\mathbf{r};t)\,, \tag{4}$$

where $\rho(\mathbf{r}')$ is the initial spin density. $G(\mathbf{r}'|\mathbf{r};t)$ is the Green's function or the propagator. It is defined as the probability for a particle at position $\mathbf{r}'$ at time 0 to diffuse to point $\mathbf{r}$ during a time t. The propagator satisfies the diffusion equation at the interior of the pore space:

$$\begin{aligned} &\frac{\partial G(\mathbf{r}|\mathbf{r}';t)}{\partial t} - D\nabla^2 G(\mathbf{r}|\mathbf{r}';t) = 0;\ \text{and} \\ &G(\mathbf{r}|\mathbf{r}';t)|_{t=0} = \delta(\mathbf{r}-\mathbf{r}')\,, \end{aligned} \tag{5}$$

where D is the diffusion constant. The boundary condition at the surface Σ:

$$D\hat{\mathbf{n}}\cdot\nabla G(\mathbf{r}|\mathbf{r}';t) + \rho\, G(\mathbf{r}|\mathbf{r}';t)|_{\mathbf{r}=\Sigma} = 0\,. \tag{6}$$

3 The Green's function in an equilateral triangular geometry

In this section we will discuss relevant eigenfunctions for situations where there is no gradients present, for the general case see Appendix 1. By using the standard eigenfunction expansion of the propagator:

$$G(\mathbf{r}|\mathbf{r}';t) = \sum_{i=0}^{\infty} \phi_i(\mathbf{r})\phi_i(\mathbf{r}')\mathrm{e}^{-t/T_i}\,, \tag{7}$$

where $\{\phi_i\}$ are an orthonormal set of eigenfunctions with corresponding eigenvalues T_i. From Eqs. 5 and 6 it then follows:

$$\begin{aligned} &D\nabla^2\phi_i(\mathbf{r}) = -\frac{1}{T_i}\phi_i(\mathbf{r}) \ \text{ and} \\ &D\hat{\mathbf{n}}\cdot\nabla\phi_i(\mathbf{r}) + \rho\,\phi(\mathbf{r})|_{\mathbf{r}=\Sigma} = 0\,. \end{aligned} \tag{8}$$

This equation needs to be solved in an equilateral triangle, shown in Fig. 1. The orthonormal set of eigenfunctions can be divided in a set of eigenfunctions symmetric and antisymmetric about the line $x = a/2$, i.e. $\{\phi\} = \{\phi^s, \phi^a\} = \{T^s/N^s, T^a/N^a\}$. $\{T^s, T^a\}$ is the set of orthogonal eigenfunctions and $N^{s,a}$ the normalization. When the magnetization is given by Eq. 4, the only relevant modes are the symmetric diagonal modes (for the full solution see Appendix 1) :

$$\begin{aligned} T^s_{ii}(x,y) &= \cos\left[\frac{2\pi\mu}{3R}y - \delta_2\right] + 2\cos\left[\frac{\pi\mu}{\sqrt{3}R}(\sqrt{3}R - x)\right]\cos\left[\frac{\pi\mu}{3R}(y-3R) + \delta_2\right] \\ T^a_{ii}(x,y) &= 0 \\ N^{s\,2}_{ii} &= \int_0^{3R}\int_{y/\sqrt{3}}^{-y/\sqrt{3}+2\sqrt{3}R} \mathrm{d}x\,\mathrm{d}y\; T^s_{ii}(x,y)\,T^s_{ii}(x,y) \\ &= \frac{9\sqrt{3}R^2}{16(\mu\pi)^2}\big\{8(1+\mu^2\pi^2) - 7\cos[2\delta_2] - 8\cos[2\mu\pi] - \cos[2\delta_2 - 4\mu\pi] \\ &\quad +8\cos[2\delta_2 - 2\mu\pi] + 4\mu\pi\sin[2\delta_2] - 16\mu\pi\sin[2\delta_2 - 2\mu\pi]\big\}, \end{aligned} \tag{9}$$

and the eigenvalues :

$$T^{-1}_{ii} = \frac{4D}{9}\left(\frac{\pi\mu}{R}\right)^2\,. \tag{10}$$

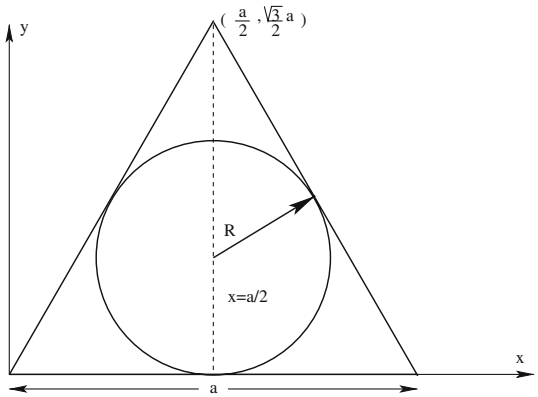

Fig. 1 Equilateral triangle of side length a and inscribed radius R

μ and δ_2 are determined from the boundary condition (8) and it give rise to the following transcendental equation:

$$\left[1-\frac{9}{2}\left(\frac{\gamma}{\pi\mu}\right)^2\right]\tan\pi\mu=\frac{9\gamma}{2\pi\mu}\,,\quad \mu\in<i,1+i]$$
$$\delta_2=\tan^{-1}\frac{3\gamma}{2\pi\mu}\text{ and }\gamma\equiv\frac{\rho R}{D}\,. \tag{11}$$

A reduced from of the propagator, when the magnetic signal is given by Eq. 4 is then:

$$G(x,y|x',y';t)=\sum_{i=0}^{\infty}\frac{T_{ii}^s(x,y)T_i^s i(x',y')}{N_{ii}^{s\,2}}\mathrm{e}^{-t/T_{ii}}. \tag{12}$$

This equation can now be used to calculate the magnetic signal from an equilateral triangular pore given an initial spin density.

4 Magnetic signal from an equilateral triangle

From Eqs. 3, 4 and 12 we find:

$$\begin{aligned}M(t)&=\mathrm{e}^{-t/T_{2b}}\sum_{i=0}^{\infty}\int\int\mathrm{d}\mathbf{r}\mathrm{d}\mathbf{r}'\rho(\mathbf{r}')\phi_i^s(\mathbf{r})\phi_i^s(\mathbf{r}')\mathrm{e}^{-t/T_{ii}}\\&=\mathrm{e}^{-t/T_{2b}}\frac{9\sqrt{3}R^2}{2}\sum_{i=0}^{\infty}\frac{\mathrm{e}^{-t/T_{ii}}}{N_{ii}^2(\mu\pi)^2}\int\mathrm{d}\mathbf{r}'\rho(\mathbf{r}')T_{ii}^s(\mathbf{r}')\big(\cos[\delta_2]\\&\quad-\cos[\delta_2-2\mu\pi]+2\mu\pi\sin[\delta_2]\big).\end{aligned} \tag{13}$$

We need to know the initial excited spin density. Usually it is assumed that the initial spin density is uniform as in the work by Brownstein and Tarr (1979). However, recently Song (2000a), Song et al. (2000b), Song (2001) and Lisitza and Song (2002) have shown during a series of papers that it is possible to create a nonuniform initial magnetization. The physical explanation for this is due to susceptibility differences between water and rock (Song 2000a, Song et al. 2000b, Song 2001, Lisitza and Song 2002). There are then four interesting cases, shown in Table 1. For the side and corner densities we have chosen points close to the surface, which lies at one of the symmetry line of the triangle. Then we only need to consider one corner (side) and the result will be equivalent for the other corners (sides).

Table 1 Different initial spin densities

Type	$\rho(x,y)$
Uniform	$1/(3\sqrt{3}R^2)$
Center	$\delta\left(x-\sqrt{3}R\right)\delta\,(y-R)$
Side	$\delta\left(x-\sqrt{3}R\right)\delta\,(y-R/32)$
Corner	$\delta\left(x-\sqrt{3}R\right)\delta\,(y-7R/32)$

$$M^{\text{uniform}}(t) = \mathrm{e}^{-t/T_{2b}} \sum_{i=0}^{\infty} \frac{27\sqrt{3}R^2}{4(\mu\pi)^4 N_{ii}^2} \mathrm{e}^{-t/T_{ii}} (\cos[\delta_2] - \cos[\delta_2 - 2\mu\pi] + 2\mu\pi \sin[\delta_2])^2 , \tag{14}$$

$$M^{\text{center}}(t) = \mathrm{e}^{-t/T_{2b}} \sum_{i=0}^{\infty} \frac{27\sqrt{3}R^2}{2(\mu\pi)^2 N_{ii}^2} \mathrm{e}^{-t/T_{ii}} \cos[\delta_2 - 2\mu\pi/3] (\cos[\delta_2] - \cos[\delta_2 - 2\mu\pi] + 2\mu\pi \sin[\delta_2]) , \tag{15}$$

$$M^{\text{side}}(t) = \mathrm{e}^{-t/T_{2b}} \sum_{i=0}^{\infty} \frac{9\sqrt{3}R^2}{2(\mu\pi)^2 N_{ii}^2} \mathrm{e}^{-t/T_{ii}} (2\cos[\delta_2 - 7\mu\pi/8] + \cos[\delta_2 - \mu\pi/4]) \times (\cos[\delta_2] - \cos[\delta_2 - 2\mu\pi] + 2\mu\pi \sin[\delta_2]) , \tag{16}$$

$$M^{\text{corner}}(t) = \mathrm{e}^{-t/T_{2b}} \sum_{i=0}^{\infty} \frac{9\sqrt{3}R^2}{2(\mu\pi)^2 N_{ii}^2} \mathrm{e}^{-t/T_{ii}} (\cos[\delta_2 - 7\mu\pi/4] + 2\cos[\delta_2 - \mu\pi/8]) \times (\cos[\delta_2] - \cos[\delta_2 - 2\mu\pi] + 2\mu\pi \sin[\delta_2]) , \tag{17}$$

where N_{ii}^2 is given in Eq. 9.

We have compared the analytical solution for the equilateral triangle with the solution for plate, cylinder and sphere, with different initial spin densities. Initial spin density close to a corner clearly does not exists for those geometries. We do not show the result for plate, cylinder and sphere here, but they behave qualitatively in the same manner. When approaching the slow diffusion limit (SDL, see next subsection) the weight of the higher modes increases compared to the uniform case, but the lowest mode always gives the highest contribution to the magnetic signal (see Fig. 2). From Fig. 2 it is evident that initial spin density close to a corner is qualitatively different from uniform, center, and side. Sharp corners and initial spin density close to the corners make the magnetic signal multiexponential very fast, even for $\gamma = 1$. For $\gamma = 4$ the lowest mode is the *least* dominant one.

In order for the lowest mode to be dominant, the spin density for all times must be more or less uniform. In the nonuniform cases, the spins lose coherence due to surface effects before the magnetization is uniform. This has the effect that nonuniform initial spin density in general makes the higher modes more dominant. In order to suppress the lowest mode, the surface effects must be felt before the spins manage to diffuse over the triangular domain to give a uniform magnetization. Clearly, corners will be very efficient of suppressing the lowest mode. This also give a natural explanation as to why this effect is not so prominent for plate, cylinder, and sphere.

4.1 Fast diffusion and slow diffusion limit

There are two different time scales of interest. The relaxation time which is dependent on the surface relaxivity, $\tau_\rho \sim R/\rho$ and the diffusion time which is dependent on the diffusion constant $\tau_{\mathrm{D}} \sim R^2/D$. If $\tau_{\mathrm{D}} \ll \tau_\rho$ we are in the fast diffusion limit (FDL) an if f $\tau_\rho \ll \tau_{\mathrm{D}}$ then we are in the slow diffusion limit(SDL). In these two limiting cases the eigenvalues and the analytical expressions for the magnetic signal simplify considerably. In the FDL the spins traverse the triangular domain many times before they relax and the magnetic decay is dominated by one mode. By simply replacing

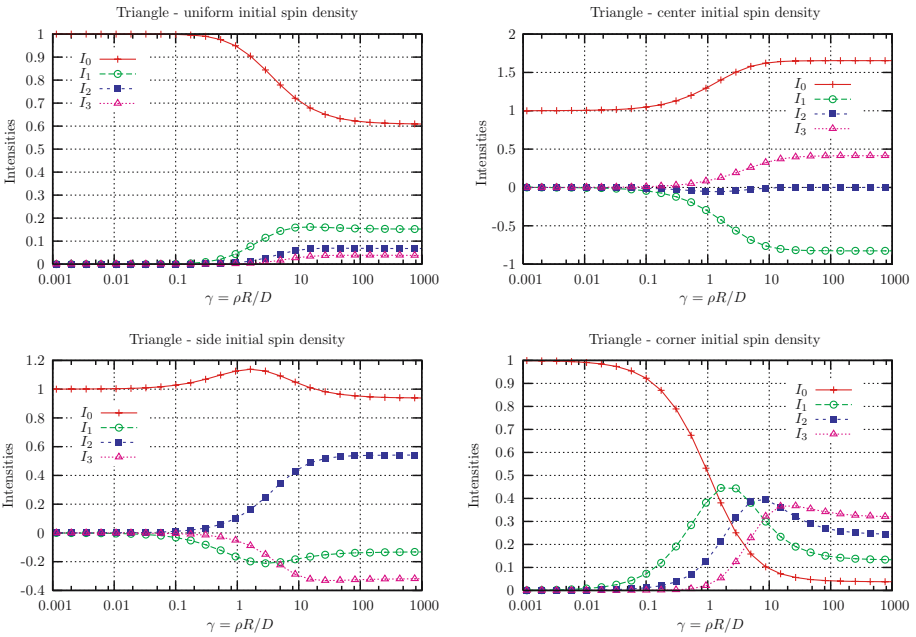

Fig. 2 Upper-left: the first four intensities for uniform initial spin density ($I_0 \to 0.61$, $I_1 \to 0.15$, $I_2 \to 0.07$, $I_3 \to 0.04$). Upper-right: the first four modes for all spins initially at the center of the triangle ($I_0 \to 1.65$, $I_1 \to -0.83$, $I_2 \to 0$, $I_3 \to 0.41$). Lower-left: the first four modes for all spins initially at the side of the triangle ($I_0 \to 0.94$, $I_1 \to -0.13$, $I_2 \to 0.54$, $I_3 \to -0.32$). Lower-right: the first four modes for all spins initially at the corner of the triangle ($I_0 \to 0.04$, $I_1 \to 0.13$, $I_2 \to 0.24$, $I_3 \to 0.32$)

tan with its argument in Eq. 11, we regain the famous result by Brownstein and Tarr (1979), by direct calculation:

$$\frac{1}{T_{00}} = \rho \frac{2}{R} = \rho \frac{S}{V}. \tag{18}$$

We write the magnetic signal from the equilateral triangle as $M(t) = \sum_i^\infty I_{ii} \exp(-t/T_{ii})$, the coefficients and eigenvalues are summarized in Tables 2 and 3. As seen from Table 3, the FDL is dominated by one mode and hence a single decay time. In Fig. 3 we have plotted the eigenvalues as a function of γ.

Table 2 Characteristic decay times as a function of surface relaxtivity , pore radius R and diffusion coefficient D in an equilateral triangle

	Fast diffusion limit $\tau_D \gg \tau_\rho$ ($\rho R/D \ll 1$)	Slow diffusion limit $\tau_D \ll \tau_\rho$ ($\rho R/D \gg 1$)
$(T_2)_{00}$	$\frac{R}{2\rho}$	$\frac{9R^2}{4D\pi^2}$
$(T_2)_{ii}$	$\frac{9R^2}{4D\pi^2 i^2}$	$\frac{9R^2}{4D\pi^2(1+i)^2}$

Note that the lowest mode is independent of the diffusion constant in FDL, while the higher modes are independent of the surface relaxtivity

Table 3 The intensities in the fast and slow diffusion limit

Note that the sum of the intensities add up to one as they should, e.g. $\sum_{i=0}^{\infty} 1/(1+i)^2 = \pi^2/6$ and $\sum_{i=0}^{\infty} \sin[2(1+i)\pi/3]/(1+i) = \pi/6$. In FDL ($\tau_\rho \gg \tau_{\mathrm{D}}$) $I_{ii} = \delta_{i,0}$ for all initial spin densities

	Slow diffusion limit
	$\tau_{\mathrm{D}} \gg \tau_\rho$ $(\rho R/D \gg 1)$
I_{ii} uniform	$\frac{6}{(1+i)^2\pi^2}$
I_{ii} center	$\frac{6\sin[2(1+i)\pi/3]}{(1+i)\pi}$
I_{ii} side	$\frac{4\sin[(1+i)\pi/8]+2\sin[7(1+i)\pi/4]}{(1+i)\pi}$
I_{ii} corner	$\frac{4\sin[7(1+i)\pi/8]+2\sin[(1+i)\pi/4]}{(1+i)\pi}$

Figures 2 and 3 show that the eigenvalues deviate faster from the FDL compared to the intensities created with an uniform initial spin density. This means that the magnetic decay is still mono exponential, but the simple relation $T_2^{-1} = \rho S/V$ is violated.

5 Numerical algorithm—random walk

In this section we will show explicitly that a random walk algorithm (Wilkinson et al. 1991, Mitra et al. 1993, Mendelson 1990, 1993, Bergman et al. 1990, Toumelin et al. 2002) gives rise to the diffusion equation (1), with the appropriate boundary condition given in Eq. 2, when the number of grid points approaches infinity. The random walk algorithm presented here will serve two purposes: (1) it will give a confirmation on the analytical results and (2) it can be extended to account for any number of phases inside a triangle. More details on scaling and convergence in random walk simulations are given in Appendix 2.

For random walk simulation in an equilateral triangle we choose a hexagonal grid (see Fig. 4). Random walkers are placed at random at a lattice point in the equilateral

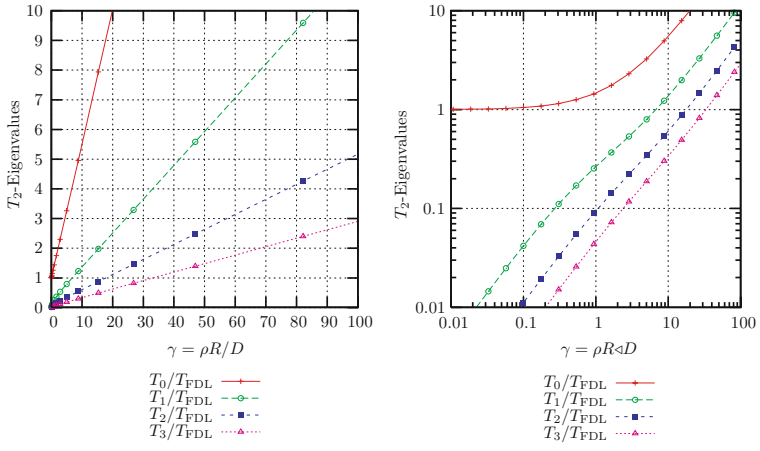

Fig. 3 Left: The eigenvalues as a function of γ, $T_{\mathrm{FDL}} = r/(2\rho)$. Right: same as left but log–log plot. For $\gamma = 0.1$ there is a 10% deviation and at $\gamma = 0.4$ there is a 20% deviation from the FDLs

triangle. The number of random walkers at an interior point r (see Fig. 4) when the clock advance one step τ is then given by

$$\begin{aligned} M(\boldsymbol{r},t+\tau)-M(\boldsymbol{r},t) = \frac{1}{6}\big[&M(\boldsymbol{r}+\epsilon\hat{\boldsymbol{i}},t)-M(\boldsymbol{r},t)+M(\boldsymbol{r}-\epsilon\hat{\boldsymbol{i}},t)-M(\boldsymbol{r},t)\\ &+M(\boldsymbol{r}+\epsilon\hat{\boldsymbol{j}},t)-M(\boldsymbol{r},t)+M(\boldsymbol{r}-\epsilon\hat{\boldsymbol{j}},t)-M(\boldsymbol{r},t)\\ &+M(\boldsymbol{r}+\epsilon\hat{\boldsymbol{k}},t)-M(\boldsymbol{r},t)+M(\boldsymbol{r}-\epsilon\hat{\boldsymbol{k}},t)-M(\boldsymbol{r},t)\big]\\ &-\kappa M(\boldsymbol{r},t). \end{aligned} \tag{19}$$

The probability for a random walker to take a step in each direction is 1/6, the probability for a random walker to die during the time step τ is κ. Dividing by τ, we find:

$$\begin{aligned} \frac{M(\boldsymbol{r},t+\tau)-M(\boldsymbol{r},t)}{\tau} = \frac{\epsilon^2}{6\tau}\Bigg[&\frac{M(\boldsymbol{r}+\epsilon\hat{\boldsymbol{i}},t)-2M(\boldsymbol{r},t)+M(\boldsymbol{r}-\epsilon\hat{\boldsymbol{i}},t)}{\epsilon^2}\\ &+\frac{M(\boldsymbol{r}+\epsilon\hat{\boldsymbol{j}},t)-2M(\boldsymbol{r},t)+M(\boldsymbol{r}-\epsilon\hat{\boldsymbol{j}},t)}{\epsilon^2}\\ &+\frac{M(\boldsymbol{r}+\epsilon\hat{\boldsymbol{k}},t)-2M(\boldsymbol{r},t)+M(\boldsymbol{r}-\epsilon\hat{\boldsymbol{k}},t)}{\epsilon^2}\Bigg]\\ &-\frac{\kappa}{\tau}M(\boldsymbol{r},t). \end{aligned} \tag{20}$$

The lattice spacing is given by ϵ. Taking the limit $\tau\to 0, \epsilon\to 0, \kappa\to 0$:

$$\frac{\partial M}{\partial t} = \frac{\epsilon^2}{6\tau}\left[\frac{\partial^2 M}{\partial i^2}+\frac{\partial^2 M}{\partial j^2}+\frac{\partial^2 M}{\partial k^2}\right]-\frac{\kappa}{\tau}M(\boldsymbol{r},t)\,. \tag{21}$$

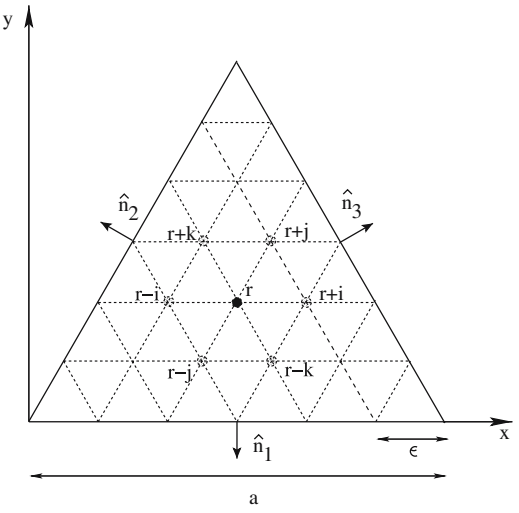

Fig. 4 Grid for random walk simulation, lattice spacing ϵ and side length a, unit outward normal vectors $\hat{\mathbf{n}}_{1,2,3}$

Changing from lattice coordinates to Cartesian coordinates:

$$\frac{\partial^2}{\partial i^2}+\frac{\partial^2}{\partial j^2}+\frac{\partial^2}{\partial k^2}=\frac{3}{2}\left(\frac{\partial^2}{\partial x^2}+\frac{\partial^2}{\partial y^2}\right), \tag{22}$$

we finally arrive at:

$$\frac{\partial M}{\partial t}=D\nabla^2 M-\frac{M}{T_{2b}}, \quad \text{where} \tag{23}$$

$$D=\frac{\epsilon^2}{4\tau} \qquad \text{and} \qquad \frac{1}{T_{2b}}=\frac{\kappa}{\tau}. \tag{24}$$

This is the same equation as (1). At a lattice point at a boundary surface normal to the $\hat{\mathbf{n}}_3$-vector (in Fig. 4), the equation becomes:

$$\begin{aligned}\epsilon\frac{M(\boldsymbol{r},t+\tau)-M(\boldsymbol{r},t)}{\tau}=&\frac{2}{3}\epsilon\frac{\epsilon^2}{4\tau}\left[\frac{M(\boldsymbol{r}+\epsilon\hat{\boldsymbol{k}},t)-2M(\boldsymbol{r},t)+M(\boldsymbol{r}-\epsilon\hat{\boldsymbol{k}},t)}{\epsilon^2}\right]\\&+\frac{2}{3}\frac{\epsilon^2}{4\tau}\frac{M(\boldsymbol{r}-\epsilon\hat{\boldsymbol{i}},t)-M(\boldsymbol{r},t)}{\epsilon}\\&+\frac{2}{3}\frac{\epsilon^2}{4\tau}\frac{M(\boldsymbol{r}-\epsilon\hat{\boldsymbol{j}},t)-M(\boldsymbol{r},t)}{\epsilon}\\&-\frac{1}{3}\frac{\zeta\epsilon}{\tau}M(\boldsymbol{r},t)\\&-\epsilon\frac{\kappa}{\tau}M(\boldsymbol{r},t)\,.\end{aligned} \tag{25}$$

We have assumed that the walkers have a probability ζ of being killed when stepping from an interior point to the wall. If a walker is not killed it is assumed to return to the interior point in the same time step. In the limit $\tau\to 0, \epsilon\to 0$, the fractions involving M are recognized to approach $\partial M/\partial t$, $\partial^2 M/\partial\epsilon^2$, $-\partial M/\partial i$ and $-\partial M/\partial j$, respectively. Using the following relation:

$$\frac{\partial}{\partial i}+\frac{\partial}{\partial j}=\sqrt{3}\,\hat{\mathbf{n}}_3\cdot\nabla \tag{26}$$

and as the LHS and the first term on the RHS in Eq. 25 are of higher order in ϵ, they can be neglected compared to the others, hence:

$$D\mathbf{n}_3\cdot\nabla M+\rho M=0 \qquad \text{and} \qquad \rho=\frac{1}{2\sqrt{3}}\frac{\zeta\epsilon}{\tau}. \tag{27}$$

By symmetry the other boundary sides give the same answer and we then regain Eq. 2.

Using the fact that number of lattice points from corner to corner along an edge is

$$N=1+a/\epsilon\,, \tag{28}$$

from Eqs. 24 and 27 we find the following important relation:

$$\gamma=\frac{\rho R}{D}=\frac{1}{3}(N-1)\zeta. \tag{29}$$

For a given γ the probability for a random walker to die when it hits the wall can be calculated from Eq. 29. Consider the ratio of bulk lattice points to surface lattice points we can define a new parameter θ, which holds the information of bulk relaxation T_{2b}:

$$\theta = \frac{N}{2}\frac{1+1/N}{(1-1/N)^2}\frac{\kappa}{\zeta} = \frac{1}{4\sqrt{3}}\frac{a}{\rho T_{2b}}\frac{N^2(N+1)}{(N-1)^3}$$
$$\xrightarrow[\epsilon\to 0]{} \frac{1}{4\sqrt{3}}\frac{a}{\rho T_{2b}} = \frac{1}{6}\frac{a^2/4D}{\gamma T_{2b}}. \tag{30}$$

The magnetic signal can then be calculated numerically by placing a number of random walkers inside the equilateral triangular domain. For uniform initial spin density the walkers are placed at random and for the delta densities all the walkers start in a point of the triangle. At each time step the walkers take one step of length ϵ and dies with a probability κ. If the walkers hit the wall they die with probability ζ. The magnetic signal will then be proportional to the number of walkers alive at each time step τ. The lattice spacing and time is related to the physical length and time by using Eqs. 24.

In Figs. 5 and 6 we have compared numerical and analytical results. There is clearly a very good match. The largest deviation between numerical and analytical results are for long times. This is natural as the number of walkers is low and the statistic is poorer. Note that if one extrapolate the straight line for high γ values in Figs. 5 (left) and 6 (left), it crosses the y-axis at $6/\pi^2$ and $6/\pi$, which is expected from Table 3. We have also made some comparison with $\theta \neq 0$, i.e. with bulk relaxation (see Eq. 30). In Fig. 7, we have plotted results for $\theta = 0.1$ and 1. For $a = 100\,\mu$m, $D = 2500\,\mu$m^2/s and $\gamma = 1, \theta = 0.1, 1$ corresponds to a bulk relaxation of 1.7 and 0.17 s respectively.

5.1 Scaling in random walk simulations

Eliminating ϵ between Eqs. 24 and 28 gives a relation between the intrinsic time scale for diffusion and the time step length in a simulation with a given N value:

$$\tau_{\mathrm{D}} \equiv \tau(N-1)^2 = \frac{a^2}{4D}. \tag{31}$$

If, for given γ and θ values, the average magnetization is plotted not against the actual time t or the integer time step counter t/τ but in units of the intrinsic time scale, viz.,

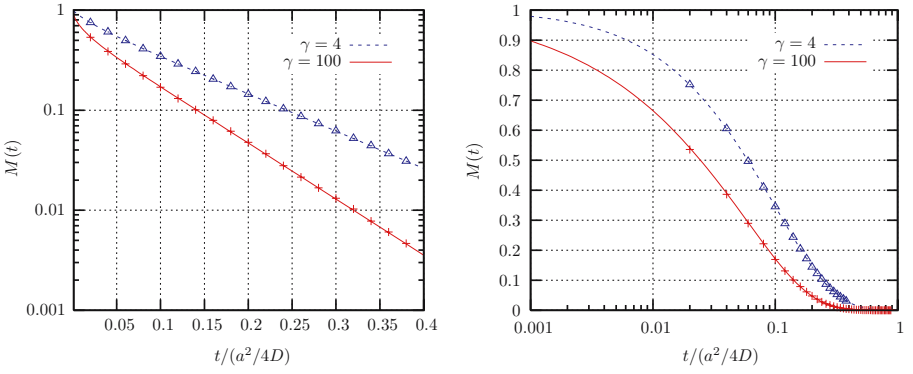

Fig. 5 Left: Comparison of random walk simulation (points) and analytical solution (line) for $\gamma = 4$ and 100. $N = 501$ and 10^6 random walkers. The initial spin density is uniform. Right: Same as left but log scale on the x-axis instead of the y-axis

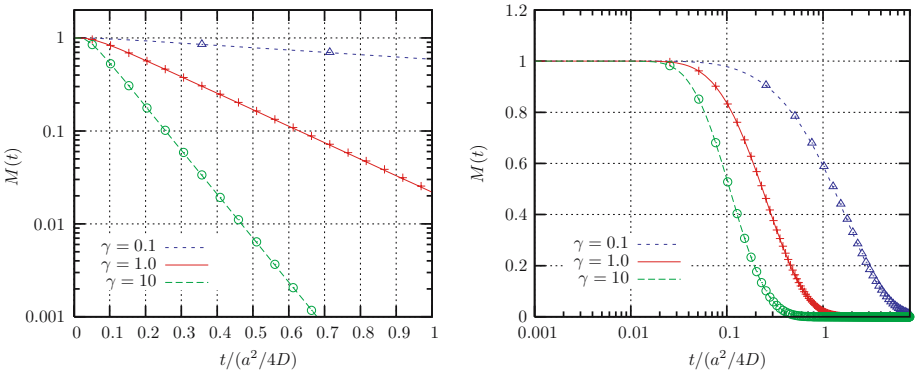

Fig. 6 Left: Comparison of random walk simulation (points) and analytical solution (line) for $\gamma = 0.1, 1$ and 10. The initial spin density is the center density. $N = 501$ and 10^6 random walkers. Right: Same as left but log scale on the x-axis instead of the y-axis

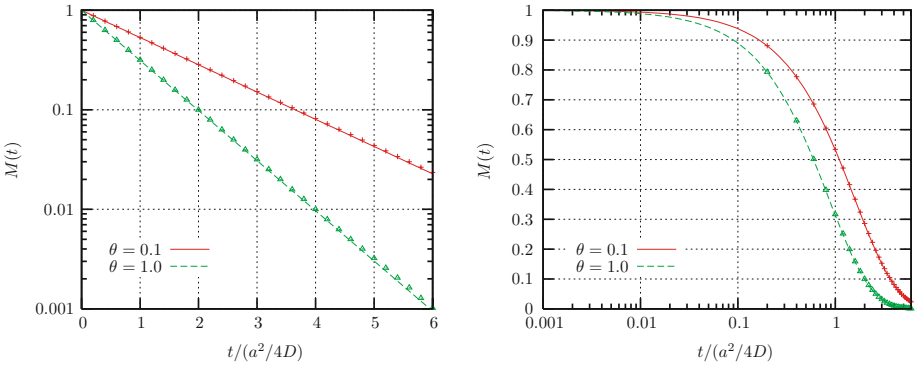

Fig. 7 Left: Comparison of random walk simulation (points) and analytical solution (line) for $\theta = 0.1, 1$, $\gamma = 1$. Uniform initially spin density, $N = 201$ and 10^6 random walkers. Right: Same as left but log scale on the x-axis instead of the y-axis

a plot against

$$\frac{t}{\tau_{\mathrm{D}}} = \frac{t}{\tau(N-1)^2},$$

then the results for various $\{N, \zeta\}$ consistent with the given γ value should be expected to plot on top of each other, provided inaccuracies due to finite N values are unimportant. This follows since $t/\tau \propto (N-1)^2$, where N is not a physical parameter but an artificial one determined by the simulation conditions. Technically, there would thus be a scaling property in the limit $N \to \infty$, in that the magnetization should depend only on a certain algebraic combination of simulation parameters.

The predicted scaling has been checked numerically for several γ values, using $\theta = 0$ (no bulk relaxation), and has indeed been found to hold. (The origins and magnitude of deviations from exact scaling is discussed in more detail in Appendix 2.) Its practical value is that for a given simulation, one may choose that set of values for $\{N, \zeta\}$ which gives an optimally acceptable combination of accuracy and computing

time requirements. This scaling is also very useful when comparing numerical and analytical results, once the results have been normalized by $t \rightarrow t/\tau_{\mathrm{D}}$ only one parameter, γ, has to be given. Pore size a, diffusion constant D and surface relaxtivity ρ are unimportant as long as the combination $\gamma = \rho R/D = \rho a/(2\sqrt{3}D)$ stay unchanged.

This scaling is also consistent with the one found by Valfouskaya et al. (2005), Valfouskaya and Adler (2005) and Valfouskaya et al. (2006). They show that for zero surface relaxtivity an universal curve exists for a porous media. It is universal in the sense that different saturations give the same curve. Considering magnetic signal from a single pore, the curve by Valfouskaya et al. reduce to the effective diffusion constant normalized by the molecular diffusion constant (D), $D_{\mathrm{eff}}(T_l)/D \equiv \langle \mathbf{r}(T_l)^2 \rangle/(4tD)$, where $T_l = 4/(9\sqrt{\pi})\sqrt{Dt}/l_s$. l_s is a typical length scale of the porous media, in our case it is $l_s = V/S = a/(4\sqrt{3})$ and $T_l = 2/(9\sqrt{\pi})\sqrt{t/\tau_{\mathrm{D}}}$, where τ_{D} is defined in Eq. 31. We have showed, in the beginning of this subsection, that once γ is fixed (and zero bulk relaxtivity) all magnetization curves, independent of the initial spin density, will plot on top of each other when the physical time has been rescaled according to $t \rightarrow t/\tau_{\mathrm{D}}$. This is exactly the type of scaling used by Valfouskaya et al. (2005), Valfouskaya and Adler (2005) and Valfouskaya et al. (2006).

6 Discussion

In pore network modeling literature, the introduction of sharp corners has shown to be very fruitful in order to understand multiphase behavior. In this article we have considered magnetic signal from one of the simplest geometries containing sharp corners, the equilateral triangle. This solution is similar to the one-dimensional geometries: plate, cylinder, and sphere in the case of uniform initial magnetization. When the initial magnetization is nonuniform the triangle behaves qualitatively different. In Song (2000a), Song et al. (2000b), Song (2001) and Lisitza and Song (2002), it was shown experimentally how to generate a nonuniform initial magnetization, due to diffusion in internal field (DDIF). A reference signal with uniform initial magnetization was used and a signal due to a nonuniform initial magnetization was created. It was seen that the nonuniform magnetization was highly multiexponential. With the triangular geometry this result can be explained by calculating the magnetic signal with uniform initial magnetization and magnetization concentrated close to the corners, shown in Fig. 8. Compared with plate, cylinder and sphere only the triangle with nonuniform initial magnetization close to the corners had a magnetic signal which behaved multiexponential for $\gamma = 1$.

In order to fully explain the experimental results generated by the DDIF technique, effect of pore connectivity (Zielinski et al. 2002) and internal gradients must also be considered. However, the results shown in Fig. 8 are very striking and they seem to capture some of the essence in the experimental results (Song 2000a, Song et al. 2000b, Song 2001, Lisitza and Song 2002).

The numerical results presented here can be extended to account for more than one phase inside the triangle. These results will then be used to study the influence of wettability on the magnetic signal and will form a basis when constructing inversion integrals used to interpret NMR-logs.

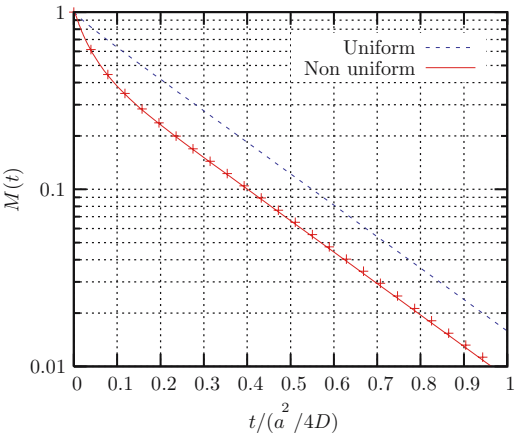

Fig. 8 Magnetic signal for uniform and corner initial spin density ($\gamma = 1$). The points are random walk calculations and lines analytical

7 Conclusion

We have presented an analytical solution for the magnetic signal from an equilateral triangular pore, with surface relaxation. To our knowledge this solution has not been presented before. This solution will be used in theoretical studies of single- and two-phase NMR response from equilateral triangles, which can be used as basic building blocks for pore scale models. This solution is also very important when interpreting experiments done at equilateral triangular tubes, which is in progress at our group.

We have studied how the magnetic signal changes for different initial conditions. For nonuniform initial magnetization the equilateral triangular geometry behaves qualitatively different than plate, cylinder and sphere due to the sharp corners.

In a forthcoming paper we will also present results for the pulsed field gradient spin echo (PFGSE) sequence (Carr and Purcell 1954, Callaghan 1991, Price 1997, 1998), the single-phase result can be calculated from the Green's function presented in this paper. Two-phase results for any value of γ must in general be solved by a random walk algorithm, except for the limit $\gamma \to 0$ where analytical results can be found. The analytical result will then serve to calibrate the numerical random walk algorithms for two-phase.

Acknowledgements The authors acknowledge ConocoPhillips and the Ekofisk Coventurers, including TOTAL, ENI, Hydro, Statoil and Petoro, for financing the work and for the permission to publish this paper from the research center COREC.

Appendix 1: The Full Green's function for an equilateral triangles

The Green's function for the equilateral triangle is given by the following equation.

$$G(x,y|x',y';t) = \sum_{i=0}^{\infty} \phi^s_{i,i}(x,y)\phi^s_{i,i}(x',y')\mathrm{e}^{-t/T_{i,i}} + \sum_{i=0}^{\infty}\sum_{j=i+1}^{\infty}\left[\phi^s_{i,j}(x,y)\phi^s_{i,j}(x',y') + \phi^a_{i,j}(x,y)\phi^a_{i,j}(x',y')\right]\mathrm{e}^{-t/T_{i,j}} \quad (32)$$

$$\phi_{i,j}^{s,a} \equiv \frac{T_{i,j}^{s,a}}{N_{i,j}^{s,a}} \quad \text{and} \quad N_{i,j}^{s,a} \equiv \int_{\Delta} \mathrm{d}x\mathrm{d}y \; T_{i,j}^{s,a}(x,y)\, T_{i,j}^{s,a}(x,y)\,. \tag{33}$$

The complete set of orthogonal eigenfunctions for the equilateral triangular triangle are (Mccartin 2004):

$$\begin{aligned} T_{ij}^{s}(x,y) = &\cos\left[\frac{\pi\lambda}{3R}(3R-y)-\delta_1\right]\cos\left[\frac{\sqrt{3}\pi(\mu-\nu)}{9R}(x-\sqrt{3}R)\right] \\ &+\cos\left[\frac{\pi\mu}{3R}(3R-y)-\delta_2\right]\cos\left[\frac{\sqrt{3}\pi(\nu-\lambda)}{9R}(x-\sqrt{3}R)\right] \\ &+\cos\left[\frac{\pi\nu}{3R}(3R-y)-\delta_3\right]\cos\left[\frac{\sqrt{3}\pi(\lambda-\mu)}{9R}(x-\sqrt{3}R)\right] \end{aligned} \tag{34}$$

$$\begin{aligned} T_{ij}^{a}(x,y) = &\cos\left[\frac{\pi\lambda}{3R}(3R-y)-\delta_1\right]\sin\left[\frac{\sqrt{3}\pi(\mu-\nu)}{9R}(x-\sqrt{3}R)\right] \\ &+\cos\left[\frac{\pi\mu}{3R}(3R-y)-\delta_2\right]\sin\left[\frac{\sqrt{3}\pi(\nu-\lambda)}{9R}(x-\sqrt{3}R)\right] \\ &+\cos\left[\frac{\pi\nu}{3R}(3R-y)-\delta_3\right]\sin\left[\frac{\sqrt{3}\pi(\lambda-\mu)}{9R}(x-\sqrt{3}R)\right]. \end{aligned} \tag{35}$$

$R = a/(2\sqrt{3})$ is the radius of the inscribed circle in an equilateral triangle of side a. The index s,a of the eigenfunctions refers to symmetric,antisymmetric about the line $x = a/2$, respectively. The complete set of orthogonal eigenfunctions is $\{T_{ij}^{s}(i \geq j);\, T_{ij}^{a}(i > j)\}$, for further details on this point see Mccartin (2004). The constants $\mu, \nu, \lambda, \delta_1, \delta_2, \delta_3$ are determined by solving the following three transcendental equations originating from the boundary condition (8):

$$\begin{aligned} \left[2L - M - N - (i+j)\pi\right]\tan L &= 3\gamma, \quad -\frac{\pi}{2} < L \leq 0 \\ \left[2M - N - L + i\pi\right]\tan M &= 3\gamma, \quad 0 < M \leq \frac{\pi}{2} \\ \left[2N - L - M + j\pi\right]\tan N &= 3\gamma, \quad 0 < N \leq \frac{\pi}{2}, \end{aligned} \tag{36}$$

where $\gamma = R\rho/D$, $i = 0, 1, \ldots$, $j = i, i+1, \ldots$ and the auxiliary variables L, M and N are related to $\mu\,, \nu\,, \delta_{1,2,3}$ in the following way:

$$\begin{aligned} &\delta_1 = L - M - N,\ \delta_2 = -L + M - N,\ \delta_3 = -L - M + N \\ &\mu = \frac{2M - N - L}{\pi} + i,\ \nu = \frac{2N - L - M}{\pi} + j,\ \lambda = -\mu - \nu\,. \end{aligned} \tag{37}$$

Finally, the eigenvalues are given by

$$T_{ij}^{-1} = \frac{2D}{27}\left(\frac{\pi}{R}\right)^2\left[\lambda^2 + \mu^2 + \nu^2\right]. \tag{38}$$

$$N^{s,a2} = \int_0^{3R}\int_{y/\sqrt{3}}^{-y/\sqrt{3}+2\sqrt{3}R} \mathrm{d}x\mathrm{d}y T_{s,a}(x,y) T_{s,a}(x,y) \tag{39}$$

in an obvious notation, the subscript i, j has been suppressed. After a rather lengthy manipulation, the result can be written:

$$N_{ij}'^2 \equiv N^{s2} = N^{a2} = F[\mu,\nu,\delta_1,\delta_2] + F[\nu,\mu,\delta_1,\delta_3] + F[\nu,-\mu-\nu,\delta_2,\delta_3] + Q[\mu,\delta_2] + Q[\nu,\delta_3] + Q[-\mu-\nu,\delta_1] \quad i \neq j, \tag{40}$$

and for $i = j$:

$$N_{ii}^{s2} = -\frac{9\sqrt{3}R^2}{16\mu^2\pi^2}\big\{-8-8\mu^2\pi^2+7\cos[2\delta_2]+8\cos[2\mu\pi] +\cos[2\delta_2-4\mu\pi]-8\cos[2\delta_2-2\mu\pi]-4\mu\pi\sin[2\delta_2] +16\mu\pi\sin[2\delta_2-2\mu\pi]\big\}. \tag{41}$$

The functions F and Q are given below:

$$F[\mu,\nu,\delta_1,\delta_2] = -\frac{3\sqrt{3}R^2}{4\mu\nu^2(\mu+\nu)\pi^2}\big\{\nu\cos[\delta_1-\delta_2](\nu+\mu\cos[2(\mu+\nu)\pi]) +(\mu+\nu)(-\nu\cos[\delta_1-\delta_2+2\mu\pi]-\mu\cos[\delta_1+\delta_2] +\mu\cos[\delta_1+\delta_2+2\nu\pi]+2\mu\nu\pi\sin[\delta_1+\delta_2]) -\sin[\delta_1-\delta_2]\sin[2(\mu+\nu)\pi]\big\} \tag{42}$$

$$Q[\mu,\delta_2] = \frac{3\sqrt{3}R^2}{8\mu^2\pi^2}\big(\cos[2(\delta_2-\mu\pi)]-\cos[2\delta_2] +2\mu\pi\big(\mu\pi-\sin[2(\delta_2-\mu\pi)]\big)\big). \tag{43}$$

Note that when $i = j$ we have $M = N$, $\delta_2 = \delta_3$, $\mu = \nu$ and $2\pi\mu = \delta_2 - \delta_1 + 2i\pi$. The eigenfunctions and transcendental equations simplifies and can after some manipulations be reduced the equations given in Sect. 3.

To summarize the Green's function for the general case can be written:

$$G(x,y|x',y';t) = \sum_{i=0}^{\infty}\frac{T_{i,i}^s(x,y)T_{i,i}^s(x',y')}{N_{ii}^2}\mathrm{e}^{-t/T_{i,i}} + \sum_{i=0}^{\infty}\sum_{j=i+1}^{\infty}\frac{1}{N_{ij}'^2}\Big[T_{i,j}^s(x,y)T_{i,j}^s(x',y')+T_{i,j}^a(x,y)T_{i,j}^a(x',y')\Big]\mathrm{e}^{-t/T_{i,j}}. \tag{44}$$

This function can be used to calculate the magnetic signal when there are gradients present in the system.

In Sect. 3 we used the fact that only the symmetric diagonal modes contribute to the magnetic signal. That the antisymmetric modes does not contribute follows by definition, but the nondiagonal symmetric modes ($i \neq j$) may give a non-vanishing contribution to the magnetic signal. To show this we integrate the symmetric modes over the equilateral triangular domain:

$$
\begin{aligned}
A &= \int_0^{3R}\int_{y\sqrt{3}}^{-y\sqrt{3}+2\sqrt{3}R} \mathrm{d}x\mathrm{d}y T_s(x,y) \\
&= -\frac{27\sqrt{3}R^2}{2\pi^2(\mu-\nu)(2\mu+\nu)(\mu+2\nu)}\Big\{(\mu-\nu)\cos[\delta_1] \\
&\quad +(\mu+2\nu)\cos[\delta_2]-(2\mu+\nu)\cos[\delta_3]+(\mu+2\nu)\cos\left[\delta_3+\frac{2\pi}{3}(\mu-\nu)\right] \\
&\quad -(2\mu+\nu)\cos\left[\delta_2+\frac{2\pi}{3}(-\mu+\nu)\right]+(\mu-\nu)\cos\left[\delta_2-\frac{2\pi}{3}(\mu+\nu)\right] \\
&\quad +(\mu+2\nu)\cos\left[\delta_1+\frac{2\pi}{3}(2\mu+\nu)\right]+(\mu-\nu)\cos\left[\delta_3-\frac{2\pi}{3}(\mu+2\nu\pi)\right]-(2\mu+\nu) \\
&\quad \times\cos\left[\delta_1+\frac{2\pi}{3}(\mu+2\nu)\right]\Big\}. \qquad (45)
\end{aligned}
$$

From Eq. 38, we find:

$$
\begin{aligned}
\mu &= -\frac{\delta_1-2\delta_2+\delta_3}{2\pi}+i \\
\nu &= -\frac{\delta_1-2\delta_3+\delta_2}{2\pi}-j. \qquad (46)
\end{aligned}
$$

We need to consider two cases separately, $j=i, j=i \mod 3 (i\neq j)$. For $j=i$ we have in addition $\delta_3=\delta_2$ $(\mu=\nu)$. We then find:

$$
A^{i=j}=\frac{9\sqrt{3}R^2}{2\mu^2\pi^2}\{\cos[\delta_2]-\cos[\delta_2+2i\pi-2\mu\pi]+2\mu\pi\sin[\delta_2]\} \qquad (47)
$$

For $j=i \mod 3 (j\neq i)$, we write $j=i+3k, k=1,2,\ldots$:

$$
\begin{aligned}
A^k &= \frac{18\sqrt{3}R^2}{(\delta_2-\delta_3-2k\pi)(-\delta_1+\delta_2+2(i+k)\pi)(-\delta_1+\delta_3+2(i+2k)\pi)} \\
&\quad \times\{(-\delta_2+\delta_3+2k\pi)\cos[\delta_1] \\
&\quad +(\delta_1-\delta_3-2(i+2k)\pi)\cos[\delta_2]+(-\delta_1+\delta_2+2(i+k)\pi)\cos[\delta_3]\}. \qquad (48)
\end{aligned}
$$

For the other cases, we find $A=0$. Using the constraints imposed by the boundary conditions (37) it turns out that $A^k=0$, this has been verified numerically by solving equation (37) for different values of $\gamma=\rho r/D$. We are then left with Eq. 47 as the final result.

Appendix 2: Random Walk

2.1 The relative importance of relaxation types

Let θ denote the ratio of bulk relaxation and boundary relaxation rates. In the fast diffusion limit, with a comparatively flat distribution of walkers, θ can be estimated by combining the ratio of bulk lattice points[1] $(N(N+1)/2)$ to boundary lattice points $(3(N-1))$ with the appropriate ratio of relaxation probabilities (a boundary walker will suffer relaxation with probability $\zeta/3$ on this lattice except in the very corner positions, where the probability is

[1] The boundary points counted among them here, since both ζ and κ small in the limit $N\to\infty$ $(\epsilon\to 0)$. If not, $(N-2)(N-3)/2$ to be used; anyway no difference in the limit $\epsilon\to 0$.

$2\zeta/3$):

$$\theta = \frac{N}{2}\frac{1+1/N}{(1-1/N)^2}\frac{\kappa}{\zeta} = \frac{1}{4\sqrt{3}}\frac{a}{\rho T_{2b}}\frac{N^2(N+1)}{(N-1)^3}$$
$$\xrightarrow[\epsilon\to 0]{} \frac{1}{4\sqrt{3}}\frac{a}{\rho T_{2b}} = \frac{1}{6}\frac{a^2/4D}{\gamma T_{2b}}. \tag{49}$$

As follows from inspection of Eqs. 23 and 27, and implicitly stated by Brownstein and Tarr Brownstein and Tarr (1977, 1979) the solutions for the average magnetization M will be three-parameter functions. In addition to γ and θ, one of the intrinsic time scales, τ_{D} for diffusion and τ_ρ for relaxation at the boundary, respectively, may be chosen as a parameter:

$$\tau_{\mathrm{D}} = \frac{a^2}{4D}$$
$$= 1.25\,\mathrm{s} \times \left(\frac{a}{0.1\,\mathrm{mm}}\right)^2 \left(\frac{2\times 10^{-5}\,\mathrm{cm}^2/\mathrm{s}}{D}\right), \tag{50}$$

$$\tau_\rho = \frac{a^2}{4D}/\gamma$$
$$= 2\sqrt{3}\frac{a}{\rho} = 17.32\,\mathrm{s} \times \left(\frac{a}{0.1\,\mathrm{mm}}\right)\left(\frac{5\,\mu\mathrm{m/s}}{\rho}\right). \tag{51}$$

One such set of parameters may thus be

$$\left\{\gamma, \frac{a^2}{4D}, \theta\right\}.$$

From Eq. 49 it follows that, physically, θ depends on the bulk sink strength density measured in units of the inverse time scale for relaxation at the boundary.

2.2 Sources and estimates of simulation inaccuracy

Figure 9 shows the results of simulations of the average magnetization M for $\gamma = 1$, in an interval of scaled time t/τ_{D}. The N values 26, 51, 101, and 201 were used; for each, 10 simulations with different random number generator seeds have been plotted, with $N_w = 10^6$ random walkers released on the lattice in each simulation. The lower most line shows the analytical solution in the same interval, plotted as the sum of 50 modes. The 'Mersenne Twister' generator (Matsumoto and Nishimura 1998, 2000) was used in this plot as random number generator, but also runs with single-precision versions of ran2 and ran3 (Press et al. 1992) were made. The simulations organize themselves in bands corresponding to the four N values used, with N increasing from above (the bands for $N = 101$ and $N = 201$ partially merging).

Various sources of error in the simulations can be discerned:

- Random:
  - Small fluctuations in the curves increase with increasing N, for the same number of random walkers.
  - Generator seed / number of walkers: With each curve showing an average over $N_w = 10^6$ walkers, for each N value there is still a seed-dependent spread within a band of the order of 0.7%.
  - Truncation errors do not give important random effects in these simulations; curves for a single-precision ran3 (not shown) have about the same variance as those shown here.

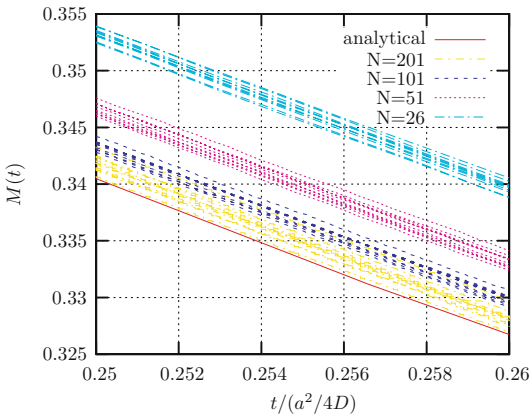

Fig. 9 (N, ζ)-dependency for $\gamma = 1, 10^6$ walkers (Mersenne Twister). Note that as N increases the numerical solution moves towards the analytical solution

- Systematic:
  - Finite ϵ effects: Since $\epsilon \propto 1/(N-1)$, choosing N too small makes the order ϵ terms in Eq. 25 increase in importance, thus violating Eq. 27 in addition to introducing inaccuracies in the representation of the derivatives in Eqs. 23 and 27. The simulation results averaged over seed values show a deviation from the analytical solution as a monotonous function of N, of order 1 % for $N = 101$ and rapidly increasing as N decreases. (Technically, these N-dependent systematic deviations may be considered a 'scaling violation'.)
  - Truncation errors: For $N = 26$ the results for ran3 (not shown) and for Mersenne Twister are very close, but for increasing N the average difference between the bands becomes larger for ran3 than for Mersenne Twister, so that for large N the bands actually make an 'undershoot' (not shown) of the analytical result. Such effects may arise from truncation when a random generator is used to make a choice with a given probability.

The level of accuracy may vary with γ and with the range of scaled time used. For the values treated above, we conclude that $N \gtrsim 200$ and $N_w \gtrsim 10^6$ should be used to obtain an accuracy in one given run of order 1 % or better.

References

Al-Mahrooqi, S., Grattoni, C., Muggeridge, A., Zimmerman, R., Jing, X.: Pore-scale modelling of nmr relaxation for the characterization of wettability. Paper presented at the 8th International Symposium on Reservoir Wettability, Houston, May 16–18, 2004

Bergman, D., Dunn, K., Schwartz, L., Mitra, P.: Self-diffusion in a periodic porous medium: a comparison of different approaches. Phys. Rev. E **51**, 3393–3400 (1990)

Brownstein, K., Tarr, C.: Importance of classical diffusion in NMR studies of water in biological cells. Phys. Rev. A **19**, 2446–2453 (1979)

Brownstein, K., Tarr, C.: Spin–lattice relaxation in a system governed by diffusion. J. Mag. Reson. **26**, 17–24 (1977)

Callaghan, P.: Principles of Nuclear Magnetic Resonance Microscopy. Oxford University Press, Oxford (1991)

Carr, H., Purcell, E.: Effects of diffusion on free precession in NMR experiments. Phys. Rev. **94**, 630 (1954)

Freedmann, R., Heaton, N., Flaum, M., Hirasaki, G., Flaum, C., Hürlimann, M.: Wettability, saturation, and viscosity using the magnetic resonance fluid characterizing method and new diffusion-editing pulse sequences. SPE **77397**, 2002 SPE Annual Technical Conference and Exhibition, San Antonio, September 29–October 2

Heaton, N., Freedman, R., Karmonik, C., Taherian, R., Walter, K., Depavia, L.: Application of a new-generation NMR wireline logging tool, SPE **77400**, 2002 SPE Annual Technical Conference and Exhibition, San Antonio, September 29–October 2

van Dijke, M., Sorbie, K.: Three-phase capillary entry conditions in pores of noncircular cross-section. J. Colloid Interface Sci. **260**, 385–397 (2003)

Helland, J., Skjæveland, S.M.: Physically based capillary pressure corelation for mixed wet reservoir from a bundle of tubes model. SPE 89428, 2004 SPE/DOE Fourteenth symposium on improved oil recovery, Tulsa, April 17–21

Helland, J., Skjæveland, S.M.: Three-phase mixed-wet capillary pressure curves from a bundle-of-triangular-tubes model. The 8th International Symposium on Reservoir Wettability, Houston, May 16–18, 2004

Howard, J.J.: Quantitative estimates of porus media wettability from proton NMR measurements. Magn. Reoson. Img. **16**, 529–533(1998)

Hui, M., Blunt, M.: Effects of wettability on three-phase flow in porous media. J. Phys. Chem. B **104**, 3833–3845 (2000)

Hürliman, M., Venkataramanan, L.: Quantitative measurement of two-dimensional distribution functions of diffusion and relaxation in grossly inhomogeneous fields. J. Mag. Reson. **157**, 31–42 (2002)

Hürlimann, M., Venkataramanan, L., Flaum, C., Speier, P., Karmonik, C., Freedman, R., Heaton, N.: Diffusion-editing: New NMR measurement of saturation and pore geometry. The 2002 SPWLA Annual Logging Symposium, Houston, June 2–5

Jackson, M., Valvatne, P., Blunt, M.: Prediction of wettability variation and its impact on waterflooding using pore- to reservoir-scale simulation. SPE **77543**, 2002 SPE Annual Technical Conference and Exhibition, San Antonio, September 29–October 2

Lisitza, M., Song, Y.: Manipulation of the diffusion eigenmodes in porous media. Phys. Rev. B **65**, 172406 (2002)

Marinelli, L., Hürlimann, M.D., Sen, P.N.: Modal analysis of q-space relaxation correlation experiments. J. Chem. Phys. **118**(19), 8927–8940 (2003)

Mason, G., Morrow, N.: Capillary behavior of a perfectly wetting liquid in irregular triangular tubes. J. Coll. Int. Sci. **141**, 262–274 (1991)

Matsumoto, M., Nishimura, T.: Dynamic Creation of Pseudorandom Number Generators, Monte Carlo and Quasi-Monte Carlo Methods 1998, pp. 56–69. Springer (2000)

Matsumoto, M., Nishimura, T.: Mersenne Twister: a 623-dimensionally equidistributed uniform pseudorandom number generator. ACM Trans. Mod. Comp. Sim. **8**, 3–30 (1998)

Mccartin, B.: Eigenstructure of the equilateral triangle, Part I: the Dirichlet problem. SIAM Rev. **45**, 267–287 (2003)

Mccartin, B.: Eigenstructure of the equilateral triangle, Part II: the Neuman problem triangle. Math. Probl. Eng. **8**, 517–539 (2002)

Mccartin, B.: Eigenstructure of the equilateral triangle. Part III. The Robin problem. IJMMS **16**, 807–825 (2004)

Meiboom, S., Gill, D.: Compensation for pulse imperfections in Carr-Purcell NMR experiments. Rev. Sci. Instrum. **29**, 688 (1958)

Mendelson, K.: Continuum and random-walk models of magnetic relaxation in porous media. Phys. Rev. B **47**, 1081–1083 (1993)

Mendelson, K.: Percolation model of nuclear magnetic relaxation in porous media. Phys. Rev. B **41**, 562–567 (1990)

Mitra, P., Sen, P., Schwartz, L.: Short time behavior of the diffusion coefficient as a geometrical probe of porous media pore geometries. Phys. Rev. B **47**, 8565–8574 (1993)

Morrow, N., Mason, G.: Recovery of oil by spontaneous imbibition. Curr. Opin. Coll. Int. Sci. **6**, 321 (2001)

Piri, M., Blunt, M.: Pore-scale modeling of three-phase flow in mixed-wet system. SPE **77726**, 2002 SPE Annual Technical Conference and Exhibition, San Antonio, September 29–October 2

Press, W. et al.: Numerical Recipes in C. Cambridge (1992)

Price, W.: Pulsed-field gradient nuclear magnetic resonance as a tool for studying translational diffusion: Part 1. Basic theory. Concepts Magn. Reson. **9**, 299–336 (1997)

Price, W.: Pulsed-field gradient nuclear magnetic resonance as a tool for studying translational diffusion: Part II. Experimental aspects. Concepts Magn. Reson. **10**, 197–237 (1998)

Radke, C., Kovscek, A., Wong, H.: A pore-level scenario for the development of mixed wettability. SPE **24880**, the 1992 Annual Technical Conference and Exhibition of the Society of Petroleum Engineers, Washington, DC, October 4–7

Song, Y.: Detection of the High Eigenmodes of Spin Diffusion in Porous Media. Phys. Rev. Lett. **85**, 3878 (2000a)
Song, Y., Ryu, S., Sen, P.N.: Determining multiple length scales in rocks. Nature **406**, 178 (2000b)
Song, Y.: Pore sizes and pore connectivity in rocks using the effect of internal field. Mag. Reson. Img. **19**, 417 (2001)
Toumelin, E., Torres-Verdin, C., Chen, S.: Modeling of multiple echo-time NMR measurements for complex pore geometries and multiphase saturations. SPE **85635**, 2002 SPE Annual Technical Conference and Exhibition, San Antonio, September 29–October 2
Valfouskaya, A., Adler, P.M., Thovert, J.-F., Fleury, M.: Nuclear-magnetic-resonance diffusion simulations in porous media. J. Appl. Phys. **97**, 083510 (2005)
Valfouskaya, A., Adler, P.M., Thovert, J.-F., Fleury, M.: Nuclear magnetic resonance diffusion with surface relaxation in porous media. J. Coll. Int. Sci. **295**, 188 (2006)
Valfouskaya, A., Adler, P.M.: Nuclear-magnetic-resonance diffusion simulations in two phases in porous media. Phys. Rev. E **72**, 056317 (2005)
van Dijke, M., Sorbie, K.: Three-phase capillary entry conditions in pores of noncircular cross-section. J. Colloid Interface Sci. **260**, 385–397 (2003)
Wilkinson, D., Johnson, D., Schwartz, L.: Nuclear magnetic relaxation in porous media: the role of the mean lifetime $\tau(\rho, D)$. Phys. Rev. B **44**, 4960–4973 (1991)
Zhang, Q., Huang, C., Hirasaki, G.: Interpretation of wettability in sandstones With NMR analysis. Petrophysics **41**(3), 223–233 (2000)
Zielinski, L.J., Song, Y., Ryu, S., Sen, P.N.: Characterization of coupled pore systems from the diffusion eigenspectrum. J. Chem. Phys. **117**, 5361 (2002)